



PERGAMON

Available online at www.sciencedirect.com

SCIENCE @ DIRECT®

Acta Astronautica 56 (2005) 573–591

ACTA
ASTRONAUTICA

www.elsevier.com/locate/actaastro

On-board entry trajectory planning for sub-orbital flight

Zuojun Shen¹, Ping Lu*

Department of Aerospace Engineering, Iowa State University, 2271 Howe Hall, Ames, IA 50011-2271, USA

Received 25 April 2003; received in revised form 6 August 2004; accepted 19 October 2004

Abstract

An algorithm for on-board planning of sub-orbital entry trajectories is presented. For entry vehicles with low lift-to-drag ratios and entering entry flight at sub-orbital speeds, this algorithm fills a gap left in a recently developed methodology for on-board generation of three-degree-of-freedom (3DOF) entry trajectories. The algorithm developed in this paper is able to reliably generate a 3DOF feasible sub-orbital entry trajectory in a time frame compatible with on-board environment. The combination of this algorithm and an algorithm recently developed for orbital entry missions provides the capability for full-envelope autonomous adaptive entry guidance. The current algorithm is validated by extensive high fidelity simulations using a sub-orbital reusable launch vehicle model and difficult mission scenarios including failures and aborts.

© 2004 Elsevier Ltd. All rights reserved.

1. Introduction

The traditional lifting entry guidance design, exemplified by the Space Shuttle entry guidance concept, [1] relies on two main components. One is the planning of a reference drag profile on the ground before mission. The other is on-board closed-loop tracking of the reference drag profile. The off-line reference planning addresses the requirements of thermal considerations, loads and range. When the mission changes, the reference drag profile is re-generated in mission planning according to the new conditions. During the entry flight, the drag profile can be adjusted within

certain range according to the actual range condition. While highly successful in nominal operations when systems function as expected and the sequence of events is well planned, this approach would severely restrict the options that the vehicle has in aborts and other emergency situations because of the limitation of the pre-loaded reference profile. In recent years, a number of methods have been investigated that aim at on-board design of the reference trajectory/profile for entry guidance [2–5]. In the most recent related work by the authors, [6] an algorithm is developed to generate on-board a three-degree-of-freedom (3DOF) constrained reference trajectory that satisfies all the trajectory constraints for orbital entry flight and control authority limits. A centerpiece of that algorithm is the use of the so-called quasi-equilibrium glide condition (QEGC) in lifting entry at high speeds. But the range of flight conditions in which the QEGC is valid

* Corresponding author.

E-mail address: plu@iastate.edu (P. Lu).

¹ Postdoctoral Research Associate.

depends on the lifting capability of the vehicle. For vehicles with medium or higher lift-to-drag (L/D) ratios, such as the Shuttle, the range could cover the entire entry flight. For vehicles with low L/D ratios, however, the QEGC is usually valid above certain cut-off velocity (e.g., Mach 6–8). For this class of vehicles, this limitation renders the algorithm in Ref. [6] inapplicable to sub-orbital flight, as acknowledged in the conclusions of Ref. [6].

It is the objective of this paper to fill this gap in on-board planning of entry trajectories for sub-orbital flight. While there is no magic separating line, the sub-orbital entry flight defined in this paper refers to an entry mission that begins below Mach 12. For such a mission the entry trajectories have different characteristics in that the variations of altitude and flight path angle are more rapid in most part of the trajectory. As a result, the QEGC may not be applicable or may be valid only for too short a period. Therefore a different approach is required for in-flight entry trajectory design. The need for planning sub-orbital entry trajectories can arise from flight testing of new entry vehicles, significantly off-nominal conditions, or aborts. During entry flight, unusually large environmental dispersions and vehicle modeling mismatches could cause large trajectory deviations from the nominal. In such a case it may be better off to re-design and fly a new reference trajectory starting from the current sub-orbital conditions. System failures during entry from orbit could necessitate abort to an alternate landing site, thus require the vehicle to initiate a new sub-orbital trajectory different than the original reference trajectory. In launch abort scenarios, both downrange aborts and return-to-launch-site aborts consist of an entry phase that may start at a velocity significantly lower than the orbital velocity. In aborts it is also likely that the maneuver/control ability of the vehicle is impaired by the failures that caused the abort. The capability to autonomously re-design on-board a reference entry trajectory to adapt to the current conditions, alternate landing site if necessary, and the current maneuverability of the vehicle is crucial for the safe return of the crew and vehicle.

This paper presents an approach for on-board planning of 3DOF reference entry trajectories for sub-orbital missions. The combination of the current algorithm and the algorithm in Ref. [6] for on-board orbital

entry trajectory design completes the trajectory planning capability of an autonomous entry guidance system throughout the entry flight envelope. While this sub-orbital entry trajectory planning algorithm shares some elements of heritage from the algorithm in Ref. [6], it should be stressed that this algorithm differs significantly in a number of major respects because the QEGC is no longer used here (see Section 3.1 for detailed comparison). Some of the primary driving factors in design of sub-orbital entry trajectories also differ from those for orbital entry flight. Since sub-orbital flight is much shorter, and thermal constraints are usually not active any more, the main requirement for the reference trajectory is feasibility, meaning that it must be intrinsically flyable, and satisfy all the boundary conditions imposed. The key ingredients in the algorithm proposed include dividing the trajectory into a constant bank-angle phase, an analytical representation phase, and an optional final refinement update that further reduces terminal condition errors. In the analytical representation phase the altitude-versus-velocity profile is represented by a polynomial. This polynomial is carefully constructed so that its flyability is maximized. Two sequential one-parameter searches are the main iterations, one for the bank angle magnitude of the constant bank phase, and the other for the point where the bank angle begins to reverse its sign (referred to as bank reversal). Extensive tests using high fidelity simulations with the model of the X-33, a sub-orbital reusable launch vehicle, have been conducted to verify the algorithm. The algorithm converges in a fraction of 1 s on a desktop computer. Some of the test scenarios presented in this paper include 6DOF Monte Carlo simulations of trajectories under all commonly examined dispersions, and scenarios involving engine-out aborts and control surface actuator failure. The entry guidance system with the on-line trajectory planning capability succeeds in all these tests in guiding the vehicle safely to the landing site.

2. Problem statement

2.1. Equations of motion

The equations of motion are the same for both orbital and sub-orbital entry flight. For sub-orbital entry

trajectory design purposes, the Coriolis acceleration terms related to the Earth rotation can be safely ignored. The standard 3DOF point-mass dynamics of an entry vehicle over a non-rotating spherical Earth are described by the following dimensionless equations of motion [7]

$$\dot{r} = V \sin \gamma, \quad (1)$$

$$\dot{\theta} = \frac{V \cos \gamma \sin \psi}{r \cos \phi}, \quad (2)$$

$$\dot{\phi} = \frac{V \cos \gamma \cos \psi}{r}, \quad (3)$$

$$\dot{V} = -D - \frac{\sin \gamma}{r^2}, \quad (4)$$

$$\dot{\gamma} = \frac{1}{V} \left[L \cos \sigma + \left(V^2 - \frac{1}{r} \right) \left(\frac{\cos \gamma}{r} \right) \right], \quad (5)$$

$$\dot{\psi} = \frac{1}{V} \left[\frac{L \sin \sigma}{\cos \gamma} + \frac{V^2}{r} \cos \gamma \sin \psi \tan \phi \right], \quad (6)$$

where r is the radial distance from the center of the Earth to the vehicle, normalized by the radius of the Earth $R_0 = 6378$ km. The longitude and latitude are θ and ϕ , respectively. The Earth-relative velocity V is normalized by $V_c = \sqrt{G_0 R_0}$ with $G_0 = 9.81$ m/sec². The terms D and L are the aerodynamic drag and lift accelerations in g's, i.e., $D = \rho (V_c V)^2 S_{\text{ref}} C_D / (2mG_0)$ and $L = \rho (V_c V)^2 S_{\text{ref}} C_L / (2mG_0)$, where ρ is the atmospheric density, S_{ref} the reference area of the vehicle, and m the mass of the vehicle. Note that D and L are also functions of α , the angle of attack, through the dependence of the drag and lift coefficients C_D and C_L on α . The flight path angle is γ and σ the bank angle. The velocity azimuth angle ψ is measured from the North in a clockwise direction. The differentiation is with respect to the dimensionless time $\tau = t / \sqrt{R_0 / G_0}$.

2.2. Trajectory constraints

For discussion purposes, horizontal landing of the vehicle is assumed in this paper, although the methodology developed here will have no difficulty to apply to vertical landing. The reference entry trajectory designed on-line should start at the current conditions, and terminate at a specified distance from the landing site where the guidance is handed over to the

terminal area energy management (TAEM) guidance system. At the TAEM interface, the entry trajectory must have correct conditions to ensure that successful TAEM and approach/landing flight is possible. These requirements form the terminal conditions for the entry trajectory as

$$r_f = r_{\text{TAEM}}, \quad (7)$$

$$V_f = V_{\text{TAEM}}, \quad (8)$$

$$s_f = s_{\text{TAEM}}, \quad (9)$$

where s_f is the final value of range-to-go s_{togo} , defined to be the range from the vehicle position to the center of the heading alignment cone (HAC) near an end of the runway. The coordinates of the center of the HAC are known. The TAEM altitude r_{TAEM} , velocity V_{TAEM} and range-to-HAC s_{TAEM} are all specified for a given vehicle. In addition, the Earth-relative velocity vector at the TAEM interface should be pointing to the HAC. Let $\Delta\psi_f$ be the difference between the velocity azimuth angle and the line-of-sight angle from the vehicle to the HAC at the TAEM interface. The condition of correct heading at the TAEM interface is then represented by

$$|\Delta\psi_f| \leq \Delta\psi_{\text{TAEM}}. \quad (10)$$

This condition stipulates that the final velocity vector should be directed at the HAC within a given tolerance $\Delta\psi_{\text{TAEM}}$.

The bank angle magnitude at the TAEM interface often times is also another parameter required not to be excessively large. Too large a σ_f could result in large transient response for the TAEM guidance and control. Thus, the constraint

$$|\sigma_f| \leq \sigma_{\text{TAEM}} \quad (11)$$

for a given $\sigma_{\text{TAEM}} > 0$ may also be imposed.

While heating constraint is no longer a primary concern for sub-orbital flight, other path constraints may still be desired to be observed, including

$$|L \cos \alpha + D \sin \alpha| \leq n_{z_{\text{max}}}, \quad (12)$$

$$q \leq q_{\text{max}}. \quad (13)$$

The constraint Eq. (12) is on the aerodynamic load (in g's) in the body-normal direction. Depending on the

vehicle configuration and mission, this constraint may be replaced by the total load constraint

$$\sqrt{L^2 + D^2} \leq n_{\max}. \quad (14)$$

Constraint Eq. (13) is on the dynamic pressure with $q = \rho(V_c V)^2/2$. The parameters $n_{z_{\max}}$ (n_{\max}) and q_{\max} are vehicle-dependent constants.

2.3. Trajectory planning problem

The sub-orbital entry trajectory planning problem is defined as follows: given the initial conditions, vehicle modeling data, terminal conditions at the TAEM interface, find the state history of $\mathbf{x} = \{r \ \theta \ \phi \ V \ \gamma \ \psi\}^T$ and the corresponding trajectory control $\mathbf{u} = \{\sigma \ \alpha\}^T$ such that:

1. The state and control profiles $\mathbf{x}(t)$ and $\mathbf{u}(t)$ satisfy the 3DOF equations of motion Eqs. (1)–(6).
2. The pair $[\mathbf{x}(t) \ \mathbf{u}(t)]$, $t_0 \leq t \leq t_f$, satisfies the current flight conditions at t_0 , and all the required TAEM interface conditions at t_f as specified in the preceding section.
3. Both σ and α profiles do not exceed the flight control system authority in terms of the maximum magnitudes, rates and accelerations of σ and α .

A pair $[\mathbf{x}(t) \ \mathbf{u}(t)]$ that meets the above conditions is called a feasible trajectory. For on-board applications, the algorithm must find a feasible trajectory quickly and reliably. Two implicit assumptions are that (1) for the given conditions and vehicle model, a feasible trajectory exists; (2) the entry flight is lifting flight, i.e., $L/D \neq 0$. A nominal α -versus-velocity (or α -versus-Mach number) profile is also assumed to be available, and limited variations about this nominal profile are allowed. A nominal α profile, once determined for a given vehicle based on trim considerations and path constraints, typically does not change significantly from mission to mission.

3. Algorithm development

3.1. Overview

While a number of elegant analytical and semi-analytical results are available [7,8] that offer great

insight to some of the atmospheric flight problems, the stringent requirements on precision and fidelity of the reference trajectory for on-board guidance purposes dictate that trajectory planning problem posed here will have to be handled by a numerical approach. The key to high efficiency and reliability of the algorithm is how to convert the trajectory planning problem from an infinite-dimensional problem in the functional space to a finite-dimensional search problem that is solvable quickly. The algorithm developed in this paper generates a sub-orbital entry trajectory in two major steps plus an optional final step:

1. Design the longitudinal profiles for velocity and altitude that meet the range requirement and TAEM conditions Eqs. (7)–(9), and find the associated bank angle magnitude and angle of attack profile.
2. Search for the appropriate point where the bank angle changes its sign (bank reversal) to meet the heading offset condition Eq. (10). Complete 3DOF trajectory is obtained by integrating Eqs. (1)–(6).
3. When necessary, further improve the accuracy of the TAEM range condition (9) by slightly adjusting the angle of attack profile if the TAEM range error exceeds tolerance.

Step 1 is further divided into two phases: a constant-bank phase and an analytical representation phase. The constant-bank phase is a period where a to-be-determined constant bank angle is used. This phase serves as a transition period from the given initial conditions to the analytical representation phase, where the desired altitude-versus-velocity profile of the trajectory is approximated by a polynomial. This polynomial is designed to meet the TAEM conditions (7) and (8) and account for the path constraints when necessary. The flyability of this analytical representation will be analyzed. The value of the constant bank angle is searched so that the combination of these two phases gives the correct conditions as specified in Eqs. (7)–(9).

In Ref. [6], there is an initial descent phase for orbital entry trajectory planning where the trajectory uses a constant bank angle to descend from entry interface at 120 km to an altitude of about 85 km where the QEGC becomes valid. But the constant bank angle is not iteratively searched to meet any trajectory constraint in Ref. [6]. Here the search for the constant

bank angle constitutes one of the two sequential iterations in the algorithm and is the mechanism to ensure the satisfaction of the TAEM conditions Eqs. (7)–(9). There is also a pre-TAEM phase in Ref. [6] where a polynomial in r and V is used to construct a desired r -versus- V profile for the orbital entry trajectory near the TAEM interface. The main differences lie in the fact that the pre-TAEM phase in Ref. [6] is short, the r -versus- V polynomial is constructed only once, and the actual trajectory does not even need to follow this profile precisely. For sub-orbital entry cases, the analytical representation phase becomes a major part of the trajectory. Hence the r -versus- V polynomial must be flyable and can be followed closely. To this end, the flyability of this polynomial representation of the trajectory needs to be analyzed, and mechanism must be developed to improve the flyability when necessary. Another distinction is that this polynomial is constructed in every iteration of Step 1, connecting the altitude and velocity at the end of constant-bank phase (which change in each iteration) to those in Eqs. (7) and (8). See Section 3.2 for detail.

Step 2 is much like the corresponding part of the algorithm in Ref. [6]. In this step, another one-parameter search is iteratively performed to determine the bank reversal point while tracking the altitude-versus-range and velocity-versus-range profiles by feedback control laws in σ and α . When the correct bank reversal point is found, the integrated trajectory will have also a TAEM heading offset satisfying (10), and this will be the final generated reference trajectory (provided Step 3 is not opted).

Step 3 is optional. In some cases the error in the range condition (9) from Step 2 at the specified TAEM energy could be larger than tolerance. This error is chiefly caused by less accurate tracking of the longitudinal profiles due to the bank reversal taking place too close to the TAEM interface. In those cases the error in the range is used to adjust the angle of attack profile to reduce the TAEM range error.

The details in each step, Steps 1 and 3 in particular, are given below.

3.2. Longitudinal profiles

The longitudinal trajectory profiles are those for velocity, altitude, and the corresponding bank angle magnitude and α histories. The flight path angle profile

will then be determined from r and V through Eq. (1). These profiles should satisfy dynamic Eqs. (1), (4) and (5). Note that the sign of σ cannot be determined by the longitudinal profiles, but is left for Step 2 of the algorithm. With the assumption of small heading offset with respect to HAC, $\Delta\psi$, the range-to-HAC history is also defined from the longitudinal profile. Fig. 1 shows in the velocity-altitude space a typical sub-orbital entry trajectory, the boundaries of the path constraints (12)–(13), and the formation of the constant-bank and analytical representation phases.

3.2.1. Constant-bank phase

In this phase a constant bank angle σ_0 and the nominal α profile are used to numerically integrate the 3DOF equations of motion (1)–(6) with the given entry conditions. The sign of σ_0 is so chosen that the aerodynamic lift contributes to reduce the magnitude of $\Delta\psi$, the heading offset to the HAC. Starting from a first-cut guess of σ_0 (such as $|\sigma_0| = 40^\circ$), the integration is continued until at a point where the following condition is satisfied

$$\left| \frac{dr}{dV} - \frac{r - r_{\text{TAEM}}}{V - V_{\text{TAEM}}} \right| < \varepsilon, \quad (15)$$

where $\varepsilon > 0$ is a small preselected value, and from Eqs. (1) and (4) dr/dV is calculated by

$$\frac{dr}{dV} = \frac{V \sin \gamma}{-D - \sin \gamma / r^2}. \quad (16)$$

The condition in Eq. (15) is continuously checked during the integration. The point where (15) is met is called the transition point which marks the end of the constant-bank angle phase and the beginning of the analytical representation phase. The geometric interpretation of condition (15) is that at the transition point, the trajectory is pointing at the TAEM point in the velocity-altitude space (cf. Fig. 1). Another benefit of such a choice is to aid the flyability analysis in Section 3.2.3 later.

As will be seen in the next section, the trajectory conditions at the transition point help uniquely define a polynomial in r and V in the next phase. The computation in the next phase will also provide clear information on how σ_0 should be adjusted in order to meet the TAEM velocity constraint Eq. (8) when the range reaches condition Eq. (9). The above process is then repeated with the updated σ_0 . When the process

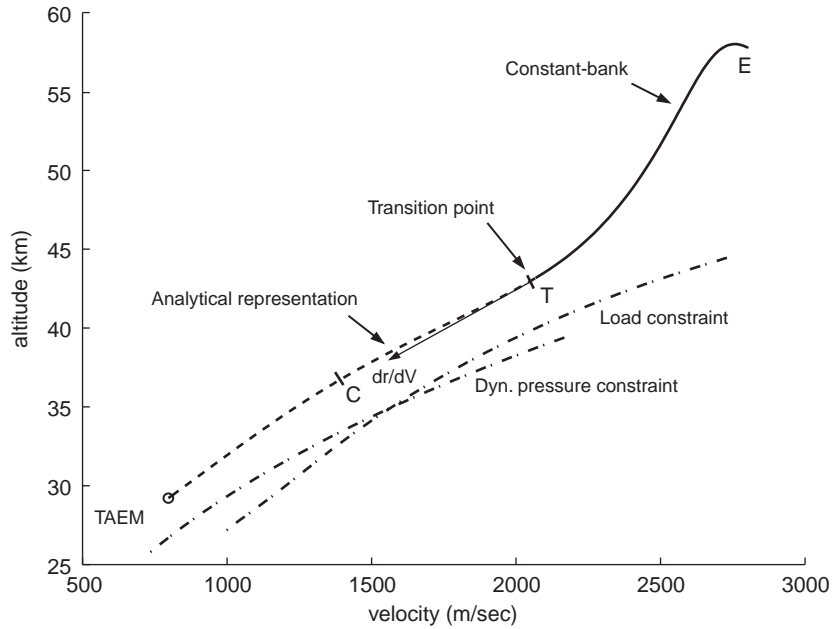


Fig. 1. A typical longitudinal profile for sub-orbital entry.

is completed, the integrated longitudinal profiles, σ_0 , and α from the entry point to the transition point, as well as the range-to-HAC history s_{togo} , are all obtained and stored for later use.

3.2.2. Analytical representation phase

In this phase a 4th order polynomial is used to represent the desired altitude-versus-velocity profile connecting the transition point to the TAEM point

$$r = a_4 V^4 + a_3 V^3 + a_2 V^2 + a_1 V + a_0. \quad (17)$$

Five conditions are needed to determine the coefficients a_i 's. Denote the known altitude and velocity at the transition point T by r_T and V_T . Let the midway point in velocity between V_T and the specified TAEM velocity V_{TAEM} be V_c , i.e.,

$$V_c = 0.5(V_{\text{TAEM}} + V_T).$$

Suppose that at V_c , the boundary of the dynamic pressure constraint (13) dominates that of the load constraint (12) as depicted in Fig. 1. Choose the altitude r_c at V_c such that the dynamic pressure at the midway point C is the average value of the dynamic pressure at point T and the TAEM point. The choice of r_c will be

based on average value of load if the load constraint dominates the dynamic pressure constraint at V_c . Such a choice of r_c ensures that the midpoint of the curve (17) in the $V - r$ space will lie above the constraint boundary, therefore the path constraint is not violated at this point.

Three sets of conditions are already given or known that will be used to determine the coefficients in Eq. (17): $(r_{\text{TAEM}}, V_{\text{TAEM}})$, (r_T, V_T) , and $(dr/dV)_T$ (the value of dr/dV at point T). The remaining two conditions will be from the values of dr/dV at the TAEM point, denoted by f_0 , and d^2r/dV^2 at the TAEM point, denoted by g_0 . When r and V satisfy Eq. (17), it is not difficult to show that the altitude at V_c can be expressed as

$$r_c = \frac{5}{16} y_1 - \frac{1}{16} x_1 f_1 + \frac{1}{4} f_0 x_1 + \frac{1}{32} g_0 x_1^2 + r_{\text{TAEM}}, \quad (18)$$

where $x_1 = V_T - V_{\text{TAEM}}$, $y_1 = r_T - r_{\text{TAEM}}$, and $f_1 = (dr/dV)_T$. The value of r_c is already chosen as described above (to produce an appropriate dynamic pressure level at V_c). Other quantities in Eq. (18) are also known except for f_0 and g_0 . On the other hand,

the vehicle dynamics dictate that $f = dr/dV$ is given by Eq. (16) and

$$g_0 = \frac{d^2r}{dV^2} \Big|_{\text{TAEM}} = \frac{1}{\dot{V}} \left(\sin \gamma + \frac{1}{\dot{V}} \dot{\gamma} V \cos \gamma \right) + \frac{\dot{r} \dot{\gamma} \cos \gamma}{r^2 \dot{V}^3} + \frac{\dot{r}}{\dot{V}^2} D_V - \frac{2\dot{r}^2 \sin \gamma}{r^3 \dot{V}^3}, \quad (19)$$

where $D_V = \partial D / \partial V$. From Eq. (16) it is clear that $f_0 = (dr/dV)_{\text{TAEM}}$ is defined if γ_{TAEM} is selected, because r_{TAEM} and V_{TAEM} are given. When replacing \dot{r} , \dot{V} and $\dot{\gamma}$ in Eq. (19) by Eqs. (1), (4) and (5), we see for the same reason that $g_0 = (d^2r/dV^2)_{\text{TAEM}}$ is dependent only on γ_{TAEM} and σ_{TAEM} . We will set σ_{TAEM} to be a relatively small value or zero to reflect the requirement of Eq. (11). Therefore both f_0 and g_0 are functions of γ_{TAEM} , and condition (18) constitutes an equation for γ_{TAEM} . Solving (18) numerically gives γ_{TAEM} , and f_0 and g_0 in turn. It should be noted that the solution process converges quickly despite the transcendental nature of Eq. (18). This is due to the fact that the term $g_0 x_1^2 / 32$ is smaller compared to other terms because $0 < x_1 < 1$ in dimensionless variables, thus close initial guess of the solution can be obtained by ignoring the term $g_0 x_1^2 / 32$ first.

Now that the desired r -versus- V profile (17) is determined, we turn our attention to the range requirement. The range-to-go to the HAC, s_{togo} , is defined to be the arc length in radian along a great circle from the current position of the vehicle to the HAC. The differential equation for s_{togo} is

$$\dot{s}_{\text{togo}} = - \frac{V \cos \gamma \cos \Delta\psi}{r}, \quad (20)$$

where $\Delta\psi$ is the heading offset angle with respect to the HAC. The usual approximation of $\cos \Delta\psi \approx 1$ proves to be still valid in sub-orbital flight. Hence combining Eq. (4) and the above equation gives

$$\frac{dV}{ds_{\text{togo}}} = \frac{r}{V \cos \gamma} \left(D + \frac{\sin \gamma}{r^2} \right). \quad (21)$$

Note that the independent variable s_{togo} is decreasing. The drag D is a dominating factor in above equation since $r \approx 1$ in dimensionless form. Also γ is no longer required to be small as usually assumed in orbital entry, a condition for the QEGC to be valid. At any given

V , r is computed from Eq. (17). The drag D then is calculated with r , V , and the nominal α profile. Finally γ is evaluated by using Eq. (16) with dr/dV obtained from differentiating Eq. (17) once with respect to V . In other word, the right-hand side of the differential equation (21) is completely defined at any given V .

The value of s_{togo} at point T , the beginning of this phase is already known from the end conditions of the constant-bank phase. The final value of s_{togo} is specified by Eq. (9). The Eq. (21) can now be numerically integrated in this interval to evaluate the end velocity at s_{TAEM} . If the end velocity is higher than the required value V_{TAEM} , it suggests that a larger value of $|\sigma_0|$ in constant-bank phase should be used. This is because a larger $|\sigma_0|$ in that phase will effectively lower the altitude r_T at the transition point. A lower r_T will then cause the curve (17) to be lower in the velocity-altitude space, which in turn increases the drag D . The net effect is that the velocity will decrease faster. The reverse is also true. The iteration involves both constant-bank phase and analytical representation phase. A bi-section algorithm will converge quickly in finding the correct σ_0 because of this monotonic functional relationship.

Once the iteration stops, the TAEM velocity condition (8) and range condition (9) are satisfied. The condition on altitude (7) is also implicitly met because r is calculated from Eq. (17) and condition (7) is used in constructing the curve (17). In addition to the obtained $r(s_{\text{togo}})$ and $V(s_{\text{togo}})$ profiles, the corresponding $\gamma(s_{\text{togo}})$ profile is again computed from Eq. (16) with dr/dV obtained by differentiating (17) once with respect to V . One more differentiation of (17) with respect to V gives d^2r/dV^2 , which together with Eq. (19) can be used to back out the bank angle magnitude profile $|\sigma(s_{\text{togo}})|$.

3.2.3. Flyability of analytical altitude-velocity profile

The analytical profile (17) is not yet a part of the final trajectory. The final trajectory for this phase is the result of numerical integration of the dynamic equations (1)–(6) with σ required to track the profile (17), as will be outlined in the next section. But for (17) to be a close approximation to the actual trajectory, the curve (17) must be flyable, at least for the most part. Flyability here means that when the altitude and

velocity of the vehicle are on the curve, the required trajectory control for the vehicle to stay on the curve is within the capability of the vehicle.

For entry flight, the chief trajectory control comes from the modulation of the bank angle. In the $r - V$ space, the effect of the bank angle appears in d^2r/dV^2 as in Eq. (19) through the presence of $\dot{\gamma}$. For fixed values of r , V , γ , and α , the range of variations of d^2r/dV^2 with respect to σ defines the flyability in longitudinal direction. We will consider the range of σ between 0° and 90° for demonstration (it is possible to have $\sigma > 90^\circ$). With the nominal α profile and for every point on the curve (17), the range of possible values of d^2r/dV^2 is limited by the values of d^2r/dV^2 corresponding to $\sigma = 0^\circ$, and $\sigma = 90^\circ$, respectively. Fig. 2 shows in dashed lines the upper and lower boundaries of d^2r/dV^2 with respect to V when r is from (17).

The physical interpretation of these boundaries is that they represent the limits of acceleration for the vehicle to pull up or dive, respectively. The solid line is the actual value of d^2r/dV^2 along the curve (17) for each V . When the solid line is inside the boundaries as shown in Fig. 2, it indicates that the vehicle has the required trajectory control capability to fly the curve (17). In Fig. 2 the solid line meets the upper boundary at the TAEM point because we set the $\sigma_{\text{TAEM}} = 0$ in constructing the curve (17).

The question to be asked is how the flyability of the profile (17) can be improved if necessary. This is done by moving the two control points T and C inside the flyability corridor if needed. Note that the TAEM point is always inside the corridor by the way the value of $g_0 = (d^2r/dV^2)_{\text{TAEM}}$ is chosen in the design of the profile. Recall that the point T is determined by the end point of the constant-bank phase, and the values of r_c and V_c at point C are determined as T is fixed. Recall also that the transition point T is selected by the condition $f_T = y_1/x_1$ (cf. Eq. (15)). With this, it can be shown that the values of d^2r/dV^2 at point T and C on the profile (17) are related by

$$\left. \frac{d^2r}{dV^2} \right|_T = \left[g_0 - \frac{6}{x_1} \left(\frac{y_1}{x_1} - f_0 \right) \right] = -2 \left. \frac{d^2r}{dV^2} \right|_C. \quad (22)$$

Between the two free parameters f_0 and g_0 , f_0 (equivalently, γ_{TAEM}) can be chosen to meet the condition (18). The above proportionality condition indicates that g_0 (alternatively, σ_{TAEM}) may be selected to move

simultaneously the values of d^2r/dV^2 at the two points T and C into the flyability corridor if necessary. Once all the three points T , C and TAEM are all inside the flyability corridor as in Fig. 2, it is likely that the entire curve representing the value of d^2r/dV^2 of the profile (17) will remain inside the corridor, given the relatively short range of V in this phase of sub-orbital flight.

3.3. Completion of the 3DOF trajectory

At this time the longitudinal profiles in the constant-bank phase and the desired longitudinal profiles based on (17) in the analytical representation phase are available. The lateral profiles and the bank reversal point remain to be determined so that the TAEM condition (10) is also met. The strategy to achieve these objectives is essentially the same as the counterpart in the algorithm in Ref. [6]. We will only outline the approach here. The reader is referred to Ref. [6] for detail.

Starting from the entry point E , linear, time-varying feedback control laws for $|\sigma|$ and α are used to track the profiles $r(s_{\text{togo}})$ and $V(s_{\text{togo}})$ obtained in Sections 3.2.1 and 3.2.2. Initially the sign of σ is the same as that of σ_0 used in the constant-bank phase. The computed σ and α are utilized to numerically integrate the dynamic equations (1)–(6). The value of range s_{togo} at the point where the bank reversal takes place is found in a one-parameter search. At this point the sign of σ is changed at the maximum allowable rate to the opposite. When the longitudinal profiles are tracked closely in this process, the three TAEM conditions (7)–(9) should be satisfied.

The conclusion of this step is marked by the finding of the bank reversal point such that the heading alignment condition (10) is met at the TAEM interface. If the TAEM range meets the condition (9) within the given tolerance at the TAEM energy specified by conditions (7) and (8), a complete 3DOF entry trajectory has been found. Because the trajectory satisfies the equations of motion, it will be intrinsically flyable.

3.4. TAEM condition precision refinement

In some minority cases when the process in the preceding section is completed, the TAEM range will have larger than acceptable errors. These errors are

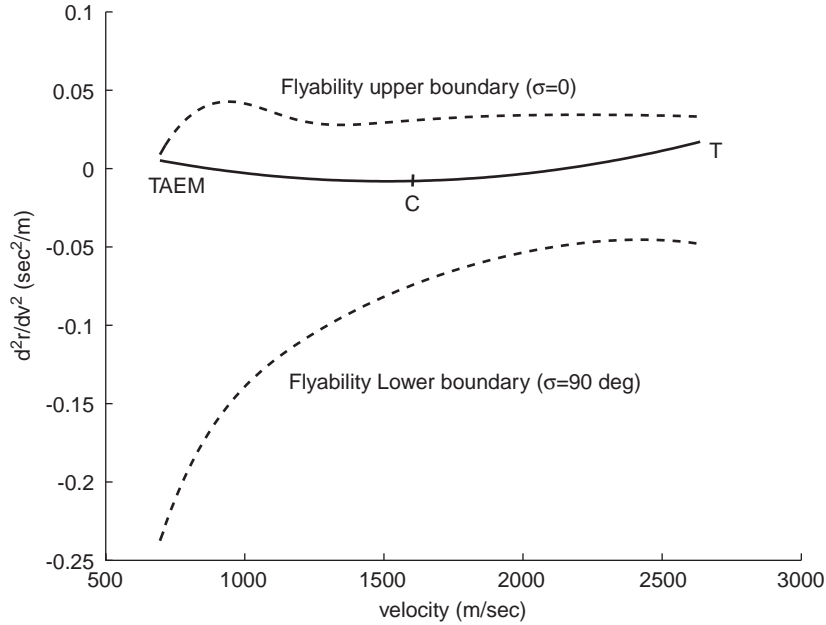


Fig. 2. Flyability corridor.

most likely to be caused by the fact that the bank reversal point is too close to the TAEM interface. During the bank reversal, the chief trajectory control σ is rate-saturated. Consequently σ renders no effective trajectory control during this period which can be considerable compared to the total entry flight time (see the example of mich10d1 mission in the next section). When the bank reversal occurs too close to the TAEM interface, the feedback control laws used to track the longitudinal profiles in Section 3.3 simply do not have sufficient time to remove the tracking errors accumulated during the bank reversal before the entry flight is terminated. In such a case it is usually futile to attempt to move the bank reversal point away from the TAEM interface, because the entry conditions and vehicle lifting capability have largely dictated where the bank reversal has to be.

Suppose that at the specified TAEM energy, there exists an unacceptable range error

$$\Delta s_f = s_f - s_{\text{TAEM}}.$$

Since this error is inherent to the problem as indicated above, it would be more effective if an appropriate bias is built into specifying the TAEM range require-

ment in trajectory planning so that, after accounting for the effects of the bank reversal, the actual range at the TAEM is s_{TAEM} as originally stipulated. The information on the case-dependent bias is already contained in Δs_f above. Thus a modified TAEM range requirement is given by

$$s'_{\text{TAEM}} = s_{\text{TAEM}} - \Delta s_f. \quad (23)$$

The longitudinal profiles found in Sections 3.2.1 and 3.2.2 with the nominal α profile will no longer meet the new TAEM range condition. The strategy of adapting to the updated s'_{TAEM} is to keep the constant-bank phase unchanged, and only modify slightly the α profile in the analytical representation phase by a constant $\delta\alpha$. Define the specific energy to be $e = 1/r - V^2/2$. It can be readily shown that

$$\frac{ds_{\text{togo}}}{de} = -\frac{\cos \gamma}{rD}, \quad (24)$$

where $\cos \Delta\psi \approx 1$ has been used. Along the already found profile (17), increasing α ($\delta\alpha > 0$) elevates the drag D , thus reduces the range, and vice versa. Hence an appropriate $\delta\alpha$ can be quickly determined using the bi-section method to accommodate the new range

condition s'_{TAEM} . The longitudinal profiles $r(s_{\text{togo}})$, $V(s_{\text{togo}})$ and $\gamma(s_{\text{togo}})$ plus $|\sigma(s_{\text{togo}})|$ and $\alpha(s_{\text{togo}})$ in the analytical representation phase are then updated accordingly.

After the above updates, the steps in Section 3.3 are repeated to complete the 3DOF trajectory. These minor updates will not alter the point of the bank reversal by appreciable extent, thus the range error characteristics remain the same. Since a corresponding range bias has been built into the longitudinal profile planning, the actual TAEM range will generally be improved to be closer to the specified value s_{TAEM} .

As a summary, Fig. 3 provides a flowchart that captures the main steps in the algorithm.

4. Algorithm tested

The test cases presented in this paper use the model and mission profiles of the X-33, a half-scale prototype of single-stage reusable launch vehicle (RLV) with a lifting-body configuration. The X-33 was to be launched from the Edwards Air Force Base (AFB) in California, USA, accelerated to about Mach 9, and then glide to land horizontally at the Michael Army Air Field (AAF) in Utah, USA. The trajectory sequence consists of ascent, transition, entry, TAEM, and approach/landing. High fidelity simulation software for the X-33, called Marshall Aerospace Vehicle Representation In C (MAVERIC), was developed at NASA Marshall Space Flight Center. Even though the X-33 program was eventually canceled, MAVERIC is continued to be used as a test bed for advanced RLV guidance and control technology development. In particular, for sub-orbital entry guidance technology assessment, a suite of 19 tests were compiled that were based on the X-33 test missions [9]. These tests include 6DOF nominal mission dispersion studies, large thrust dispersions, engine failures, control actuator failures, and significant aerodynamic modeling mismatches. The performance of the entry guidance algorithm is judged by the TAEM condition precision, observance of path constraints, thermal-structural indicators, control surface activities, and reaction control system propellant usage.

The X-33 has a relatively low L/D value of about 0.9 in the sub-orbital missions. Most of the tests are stressful and some are impossible to handle by a con-

ventional entry guidance algorithm without on-board trajectory planning capability. In fact, the baseline entry guidance algorithm for the X-33, which tracks a pre-loaded reference drag profile as in the Shuttle entry guidance, only managed to get 8.4% of the total scores, failing most of the tests where it was evaluated. Yet due to the low L/D ratio of the X-33 vehicle and the short ranges of all these missions, the algorithm developed in Ref. [6] is unable to reliably generate entry trajectories in these sub-orbital missions. In contrast, the entry guidance algorithm incorporating the trajectory planning algorithm proposed in this paper passed all the tests, and achieved overall 95% of the total scores.

Some of the test scenarios and results are presented in the following to demonstrate the performance of the algorithm.

4.1. X-33 nominal missions

Two mission profiles of the X-33 are considered. The baseline X-33 mission is called mich10a1. After the cut-off of the engines at about Mach 9, the entry flight starts following a 25-second transition period. The guidance during the transition period is open-loop. The sub-orbital entry flight lasts about 4 min. The other mission, mich10d1, is designed to delay the transition from laminar to turbulent flow, a part of an experiment to assess the properties of the thermal protection system. The open-loop transition period of mich10d1 mission is thus about 90 s long, and the closed-loop entry flight lasts for only 2 min. The nominal angle of attack profiles are different for the two missions. The nominal landing site for both missions is Michael AAF.

The TAEM conditions, path constraints, and control authority constraints are as follows:

- TAEM altitude of 29.344 km for mich10a1 and 29.438 km for mich10d1;
- TAEM range-to-HAC of 55.56 km (30 nm);
- TAEM velocity of 926 m/s for mich10a1 and 924.6 m/s for mich10d1;
- TAEM heading angle offset with respect to the HAC desired to be less than 5° , but no greater than 10° in any case;
- peak normal acceleration not to exceed 2.5 g;

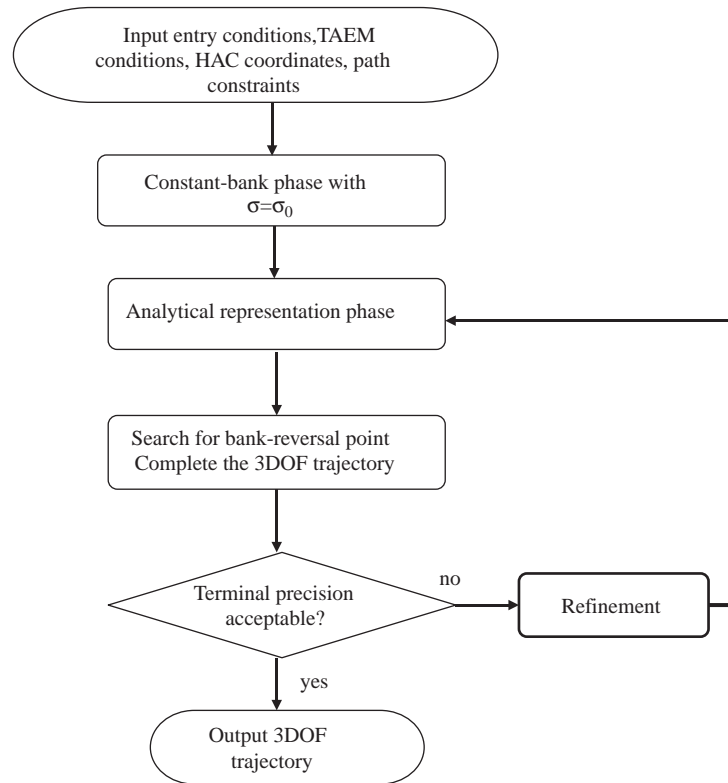


Fig. 3. Algorithm flowchart.

- peak dynamic pressure not to exceed 14,364 N/m² (300 psf);
- TAEM bank angle magnitude not to exceed 50°;
- maximum rates of 5°/s for bank angle and angle of attack;
- maximum acceleration of 3.5°/s² and 2.0°/s² for bank angle and angle of attack, respectively.

The entry trajectory planning algorithm discussed in the preceding sections was implemented as a part of the entry guidance module in MAVERIC. At the beginning of the entry flight, a 3DOF reference trajectory was generated on-line based on the current navigation data. This trajectory was subsequently tracked by the feedback guidance law described in Ref. [10]. The guidance law provided bank angle and angle of attack commands throughout the entry flight.

The 6DOF simulation results using MAVERIC are shown in Figs. 4–7 for the two missions. The X-33

baseline flight control system design was used in the 6DOF simulations. Average winds at Edwards AFB and mean winds from the Global Reference Atmospheric Model [11] (GRAM) were included in the simulations. Also plotted in these figures in dashed lines are the reference profiles generated by the trajectory planning algorithm, and, the guidance commands generated by the guidance laws in dotted lines in Figs. 5 and 7. Note that in Figs. 5 and 7 the reference bank angle and α have some differences from the commanded bank angle and α because the feedback guidance law generates the guidance commands in response to trajectory dispersions. The control system tracks the guidance commands (rather than the reference commands). As evident from the figures, the 6DOF trajectories and the 3DOF reference trajectories match quite well, given the non-trivial differences between the 3DOF and 6DOF dynamics plus the control system dynamics.

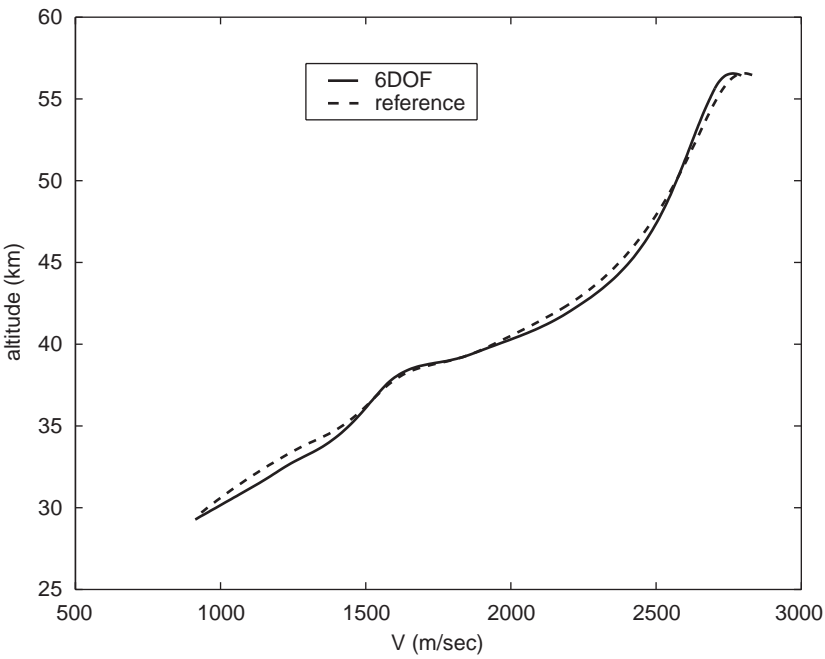


Fig. 4. Entry trajectory for mission mich10a1.

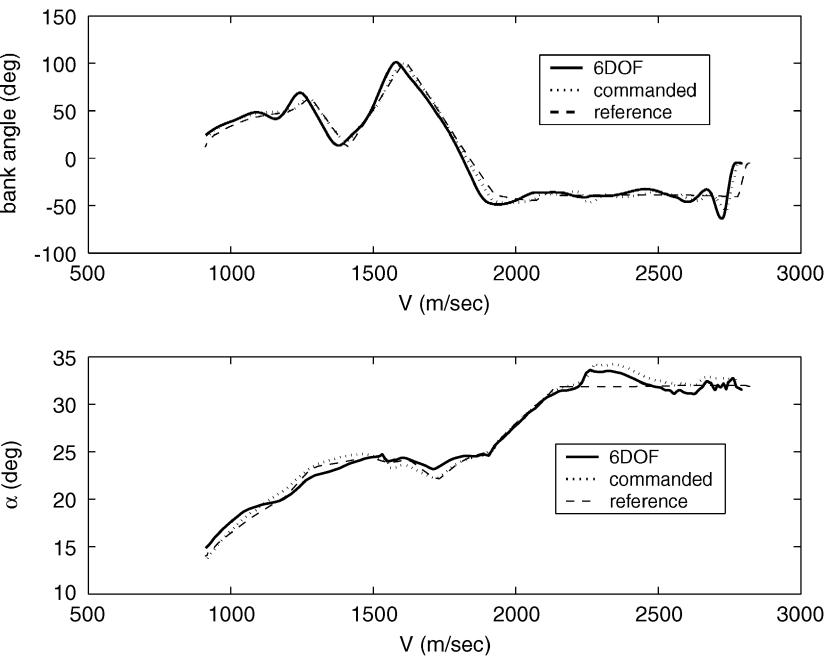


Fig. 5. Bank angle and α histories for mich10a1.

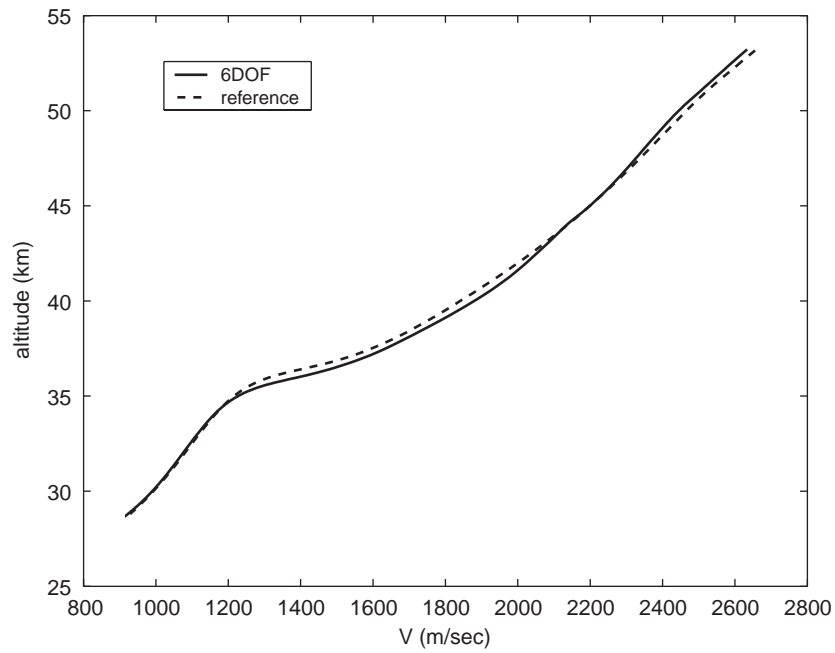


Fig. 6. Entry trajectory for mission mich10d1.

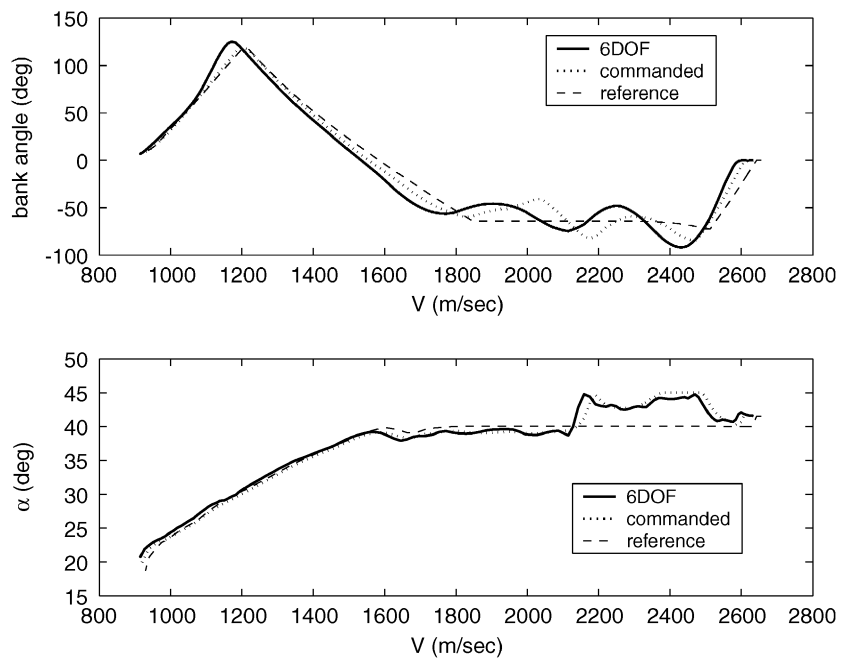
Fig. 7. Bank angle and α histories for mich10d1.

Table 1
TAEM condition precision and CPU time

Case	$\Delta\psi_f$ (°)	Δs_f (km)	Δr_f (km)	CPU time (s)
mich10a1-Ref.	−0.49	0.616	0.118	0.33
mich10a1-6DOF	0.74	1.848	−0.07	
mich10d1-Ref.	0.07	0.694	0.664	0.48
mich10d1-6DOF	0.63	−0.43	−0.76	

Some of the TAEM condition errors for both the 3DOF reference trajectories and the 6DOF simulated trajectories are listed in Table 1. The TAEM interface is reached when the Earth-relative velocity (without counting for wind velocity) is equal to the specified TAEM velocity, therefore no TAEM velocity errors are shown in Table 1. The precision levels seen in the Table 1 are excellent in the context of 6DOF entry flight. As can be observed from Figs. 5 and 7, the magnitudes of the TAEM bank angles in both cases are well within the 50° desirable range. Although not plotted in the figures or listed in the Table 1, the peak normal load and peak dynamic pressure along the 6DOF trajectories are all within their respective limits. The computation times required to generate the two reference trajectories on a 800 MHz desktop computer are also given in the Table 1. The algorithm implementation was not optimized or streamlined for efficiency. Yet in both cases the computation time is less than 0.5 s.

Monte Carlo simulations evaluate how the guidance system responds to uncertainty and dispersions. Random perturbations in propulsion force, jet effects, aerodynamic coefficients, navigation data, mass properties, winds and atmospheric properties are included in the Monte Carlo simulations. These dispersions cause the ascent trajectory to be different in each case, resulting in different entry conditions. The variations in the entry conditions can be quite appreciable, as documented by Dukeman [12]. The same uncertainties (except for those in propulsion) affect the entry flight as well. At the start of each entry flight, the entry trajectory planning algorithm generates on-line a 3DOF reference trajectory based on the actual entry conditions (hence the reference trajectory is different each time). The guidance law tracks the reference trajectory afterwards. The TAEM conditions of 100 dispersed 6DOF trajectories for each of the mich10a1

and 10d1 missions are given in Figs. 8 and 9. In Fig. 8 the values of TAEM altitude versus range-to-HAC are plotted. Any TAEM range within 5.5 km (3 nm) of the specified value and any TAEM altitude within 0.914 km (3000 ft) of the targeted TAEM altitude are considered equally good. Any TAEM range-to-HAC outside 13 km (7 nm) and altitude outside 2.134 km (7000 ft) of the respective specified values (in plus and minus directions) are regarded as failing the criteria. By these standards it can be seen that all of the dispersed cases of the 200 trajectories pass the test, and most of them are on the target. Fig. 9 shows the TAEM heading angle errors with respect the HAC versus the actual heading angle for the 200 trajectories. The figure reveals that while the trajectories for mich10a1 mission approach the HAC from different directions than those of the trajectories for mich10d1 mission, as indicated by the different final heading angles, the heading-to-HAC errors are all within $\pm 10^\circ$ range, with mich10d1 trajectories actually fairing better in this criterion. Other criteria are all well met by the majority of the trajectories. In fact, the two sets of dispersion tests score 97.2% and 95.4% out of 100% respectively when all the scoring criteria are measured.

4.2. Cases simulating system failures

Fifteen of the 19 test scenarios based on X-33 sub-orbital missions are for various cases of large thrust dispersions, engine failures, actuator failures, and substantial mismodeling of aerodynamic coefficients [9]. The goal is to evaluate the ability of the entry guidance algorithms to save the vehicle in these stressful situations. In a sense, these are the situations where a fully autonomous entry guidance system with on-board adaptive trajectory planning capability can set apart from the conventional entry guidance system.

Two of the cases to be shown here involve engine failure. The X-33 has two linear aerospike engines. Should one fail (a case of power pump out, PPO for short), the propellant can be pumped to the other engine to continue the ascent with longer ascent flight time until the propellant is burnt out. MAVERIC can simulate PPO cases as well. In a PPO case the energy at the engine burnout, consequently the energy at the beginning of entry flight, will be lower than that in the nominal flight. The dispersions in other entry conditions will also be increased. For mission

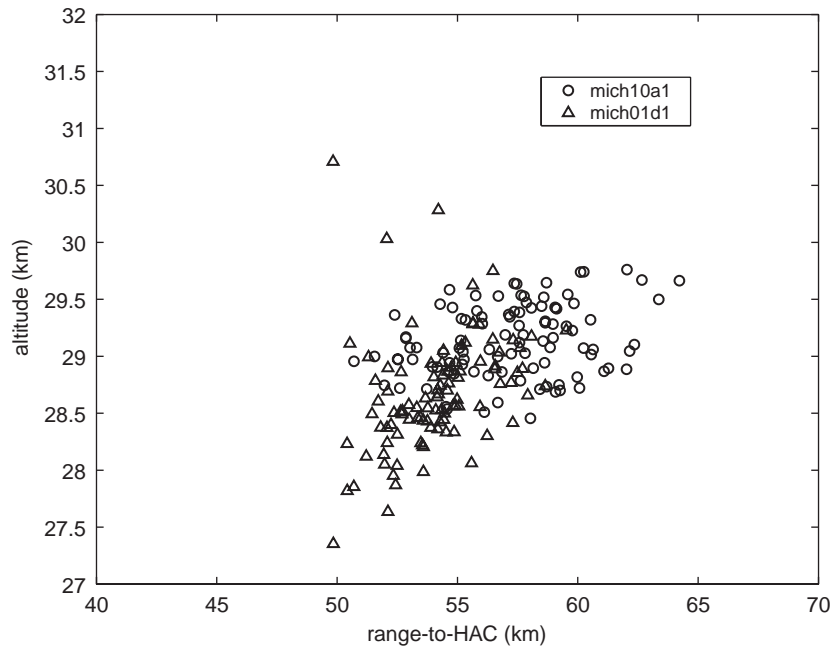


Fig. 8. TAEM altitudes and ranges for 100 dispersed mich10a1 and 100 mich10d1 trajectories.

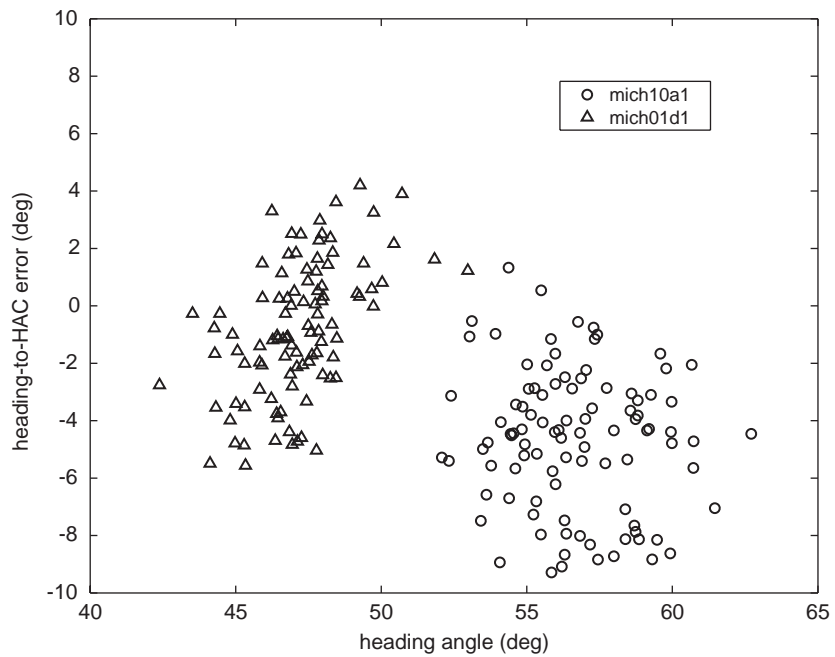


Fig. 9. TAEM heading angles and heading-to-HAC errors for 100 dispersed mich10a1 and 100 mich10d1 trajectories.

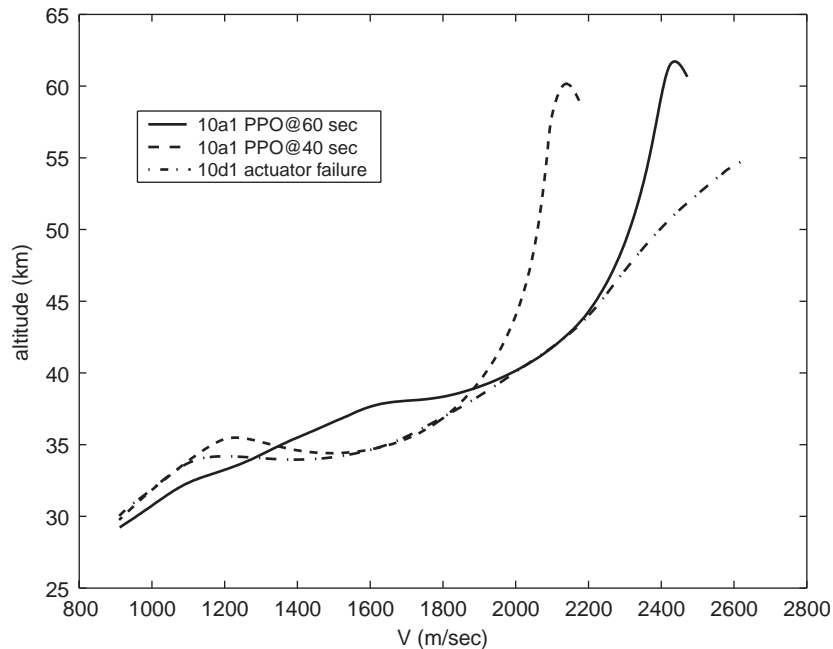


Fig. 10. Entry trajectories of three cases with system failures.

mich10a1, if PPO occurs earlier than 50 s from liftoff, the entry energy would be too low for the X-33 to reach Michael AAF as the nominal mission calls for. In such a case, a dry lake bed at Ibex Well in Utah near the Nevada border will be targeted as the emergency landing site (Ibex for short). The entry guidance system should ensure that the entry flight trajectory meets all the constraints and TAEM conditions imposed for the nominal mission, regardless of whether it is landing at Michael or Ibex. As a demonstration of the benefits of the on-board trajectory planning capability in these situations, a case of PPO at 60 s (still landing at Michael AAF) and another PPO case at 40 s (landing at Ibex), both for mission mich10a1, will be shown.

The third case is for mission mich10d1. A control surface actuator failure is assumed to have happened at the beginning of entry flight. A consequence is that the maximum bank angle rate and maximum angle of attack rate are both reduced by 20% to $4^\circ/\text{s}$. In addition, the vehicle cannot fly as high an α -profile as the nominal because of the actuator failure. The angle of attack commands to the control system will be limited

up to 5° below the nominal values. The landing site is still Michael AAF. The effects of the failure are highly stressful for entry flight in this case: the reduced bank rate increases the time needed to complete the bank reversal during which the bank angle is rate-saturated, thus provides no trajectory control to counter dispersions. The reduction of angle of attack tends to increase the magnitude of the bank angle in order to dissipate the energy, which in turn further lengthens the bank reversal time. Given the short entry flight time of only 2 min for mich10d1 mission, more than half of the entry flight duration could be spent on bank reversal maneuver. This would leave little room for the entry guidance system to effectively correct any substantial trajectory dispersions.

These three failure cases exemplify the situations where on-board entry trajectory planning capability could make a difference between mission success and failure. The trajectory planning algorithm discussed in this paper proves to be instrumental in achieving mission success in 6DOF MAVERIC simulations. In the case of system failure, the entry guidance system is informed of the failure from the vehicle health

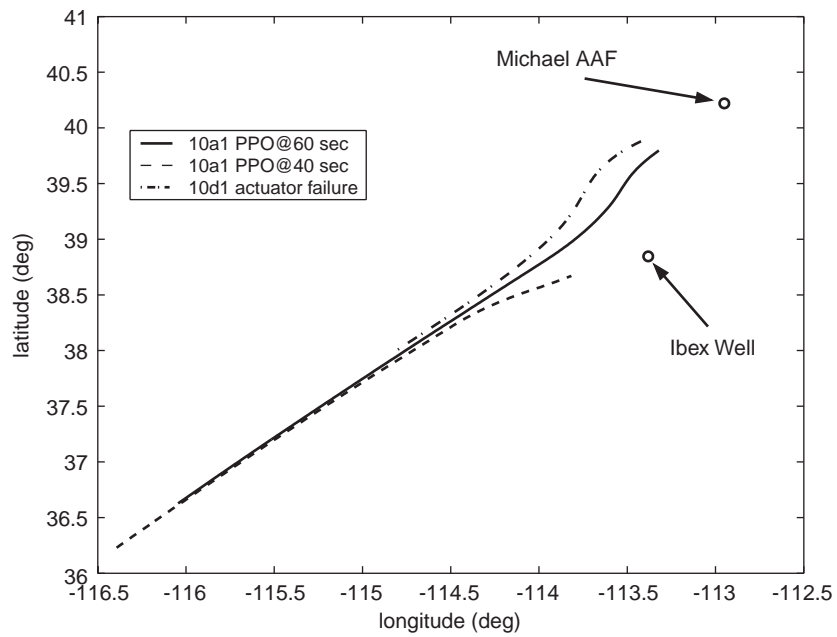


Fig. 11. Ground tracks of the entry trajectories with system failures.

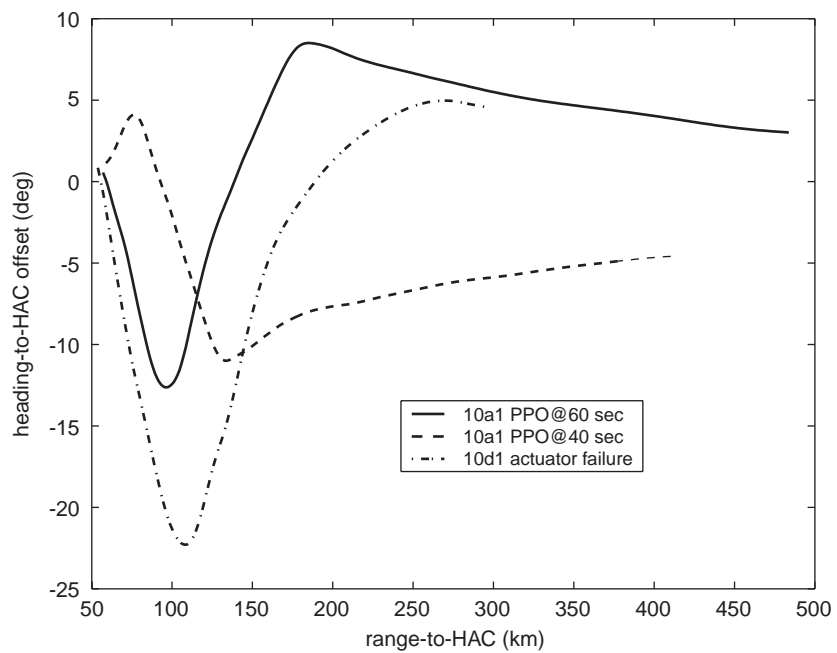


Fig. 12. Heading angle offset with respect to HAC of the entry trajectories with system failures.

Table 2
TAEM condition precision (6DOF) for cases with system failures

Case	$\Delta\psi_f$ ($^\circ$)	Δs_f (km)	Δr_f (km)	($^\circ$)
mich10a1 PPO@60 sec	0.55	1.417	-0.11	14.1
mich10a1 PPO@40 sec	0.99	-0.001	0.399	-25.3
mich10d1 w/actuator failure	1.03	-2.137	0.595	34.1

monitoring system. The entry trajectory is then generated on-line based on the current entry conditions, the targeted landing site (nominal or alternate), and the reduced control authority of the vehicle in case of actuator failure.

Fig. 10 shows the 6DOF altitude-versus-velocity histories of the entry trajectories for the three cases. Notice that for PPO at 60 s, the entry velocity is about 380 m/s lower than that of the nominal mich10a1 mission as seen in Fig. 4, a reduction of about 14%. The two PPO mich10a1 entry trajectories begin with positive flight path angles therefore the altitude keeps increasing before descent starts, a phenomenon not seen in

orbital entry. For PPO at 40 s, the entry energy (velocity) is even lower hence landing at a closer site (Ibex) is necessary. Fig. 11 illustrates the ground tracks of the three entry trajectories and clearly shows to which landing site a trajectory is heading. The shorter range to Michael AAF of mich10d1 mission is evident. Note that the final ranges are all close to the required value of 55.56 km, and the largest final heading offset is only 1° among all the cases, as can be seen from Fig. 12 in which the histories of heading offset with respect to the HAC versus range-to-HAC are plotted. Table 2 summarizes the TAEM conditions errors for the three cases in 6DOF simulations. Compared to the required values as stated earlier, the TAEM conditions are met remarkably well, given the severity of the failures.

Finally Fig. 13 depicts the variations of bank angle for the three entry trajectories where the time is counted from launch (so the abscissa starts at about 310 s). Particularly revealing is the bank history for mich10d1 mission with actuator failure. The total entry flight time is about 120 s, but half of it is needed just for the bank reversal at reduced maximum bank

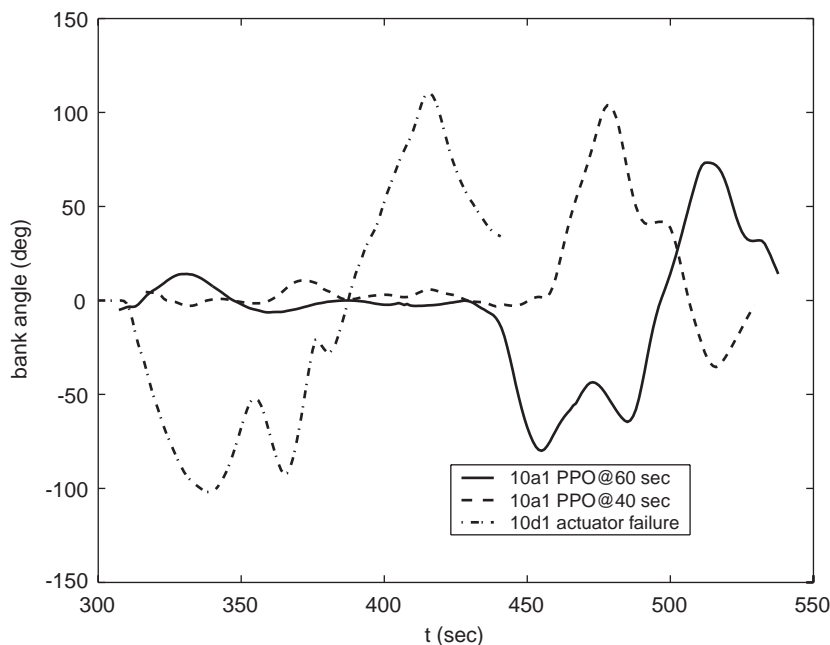


Fig. 13. Bank angles along the entry trajectories with system failures.

rate. Coupled with reduced angle of attack, this characteristics makes it significantly more difficult for the entry guidance system to achieve accurately the required TAEM conditions. In fact it is impossible to fly the nominally designed mich10d1 reference trajectory in this case. Without an on-board trajectory planner that designs a reference entry trajectory specifically tailored to the current situation, it would be highly unlikely for any entry guidance system to successfully guide the vehicle for a safe landing should this failure happen to mich10d1 mission.

5. Conclusions

A method for rapid planning of sub-orbital entry trajectories is developed. The algorithm is suited for handling entry trajectory planning for vehicles with low L/D ratios and beginning entry flight at speeds substantially lower than the orbital speed. These are the cases where an recently developed algorithm for planning orbital entry trajectories is not applicable. The current algorithm generates reliably a complete feasible three-degree-of-freedom sub-suborbital entry trajectory within a fraction of 1 s on a desktop computer, making it suitable for on-board applications. Extensive high-fidelity simulations using a reusable launch vehicle model and different mission scenarios have validated the effectiveness and reliability of the algorithm. Some of the simulation scenarios involving aborts and failures are so stressful that it would not be possible to ensure safe landing without re-planning on-board the reference entry trajectory. The combination of this algorithm and the recent algorithm for rapid trajectory generation for orbital entry missions provides the capability for full-envelope on-board entry trajectory planning. Such a capability could make future space

transportation systems safer, more adaptive and cost effective.

References

- [1] J.C. Harpold, C.A. Graves, Shuttle entry guidance, *The Journal of the Astronautical Sciences* 27 (1979) 239–268.
- [2] J.D. Gamble, C.J. Cerimele, T.E. Moore, J. Higgins, Atmospheric guidance concepts for an aeroassisted experiment, *The Journal of the Astronautical Sciences* 36 (1988) 45–71.
- [3] C. Zimmerman, G. Dukeman, J. Hanson, An automated method to compute orbital re-entry trajectories with heating constraints, *Journal of Guidance, Control, and Dynamics* 26 (2003) 523–529.
- [4] K.D. Mease, D.T. Chen, P. Teufel, H. Schoenenberger, Reduced-order entry trajectory planning or acceleration guidance, *Journal of Guidance, Control, and Dynamics* 25 (2002) 257–266.
- [5] A.J. Roenneke, Adaptive on-board guidance for entry vehicle, AIAA Paper 2001-4048, Guidance, Navigation, and Control Conference, Montreal, Canada, August 6–9, 2001.
- [6] Z. Shen, P. Lu, On-board generation of three-dimensional constrained entry trajectories, *Journal of Guidance, Control, and Dynamics* 26 (2003) 111–121.
- [7] N.X. Vinh, A. Busemann, R.D. Culp, *Hypersonic and Planetary Entry Flight Mechanics*, The University of Michigan Press, Ann Arbor, MI, 1980, pp. 26–27.
- [8] N.X. Vinh, *Optimal Trajectories in Atmospheric Flight*, Elsevier Scientific Publishing Company, Amsterdam, 1981.
- [9] J. Hanson, Advanced guidance and control project for reusable launch vehicles, AIAA Paper 2000-3957, Guidance, Navigation, and Control Conference, Denver, CO, USA, August 14–17, 2000.
- [10] P. Lu, Regulation about time-varying trajectories: precision entry guidance illustrated, *Journal of Guidance, Control, and Dynamics* 22 (1999) 784–790.
- [11] C.G. Justus, D.L. Johnson, *The NASA/MSFC Global Reference Atmospheric Model: 1999 Version (GRAM-99)*, NASA TM-209630, May 1999.
- [12] G.A. Dukeman, Profile-following entry guidance using linear quadratic regulator theory, AIAA Paper 2002-4457, Guidance, Navigation, and Control Conference, Monterey, CA, USA, August 5–8, 2002.